Structure of METTL3-METTL14 with an m6A nucleotide reveals insights into m6A conversion and sensing

Shan Qi
University of Texas Health Science Center   https://orcid.org/0000-0003-0175-6267

Abhay Kumar
https://www.researchsquare.com/article/rs-3150186/v1

Shuang Chen
University College London

Shuo Zhou
University of Texas Health Science Center

Manish Parihar
parihar@uthscsa.edu

Carmen Villalobos
University of Texas Health Science Center at San Antonio

Navom Gupta
University of Texas Health Science Center at San Antonio

Siu-Hong Chan
New England Biolabs

Manjeet K. Rao
University of Texas Health Science Center at San Antonio

Stanton F. McHardy
University of Texas San Antonio

Shozeb Haider
University College London

Yogesh K. Gupta
guptay@uthscsa.edu

University of Texas Health Science Center at San Antonio   https://orcid.org/0000-0001-6372-5007

Research Article

Additional Declarations: The authors declare potential competing interests as follows: Y.K.G is the founder of Atomic Therapeutics. S-H.C. is an employee of New England Biolabs. These affiliations do not affect the authors's impartiality and adherence to the journal's standards.

Structure of METTL3-METTL14 with an m6A nucleotide reveals insights into m6A conversion and sensing

Shan Qi[1,2], Abhay Kumar[1,2], Shuang Chen[3], Shuo Zhou[2], Manish Parihar[1,2], Carmen Villalobos[1,2], Navom Gupta[1,2], Siu-Hong Chan[4], Manjeet K. Rao[1], Stanton F. McHardy[5], Shozeb Haider[3], Yogesh K. Gupta[1, 2*]

[1] Greehey Children's Cancer Research Institute, University of Texas Health Science Center at San Antonio, 8403 Floyd Curl Drive, San Antonio, TX 78229, USA

[2] Department of Biochemistry and Structural Biology, University of Texas Health Science Center at San Antonio, 7703 Floyd Curl Drive, San Antonio, TX 78229, USA

[3] Department of Pharmaceutical and Biological Chemistry, School of Pharmacy, University College London, London, United Kingdom

[4] New England Biolabs, 240 County Road, Ipswich, MA, 01938, USA

[5] Center for Innovative Drug Discovery, Department of Chemistry, University of Texas at San Antonio, San Antonio, TX, USA

*Corresponding author:

Y.K.G. email: guptay@uthscsa.edu

Abstract

The nuclear METTL3-METTL14 transfers a methyl group from SAM to convert the N^6 of adenosine (A) in RNA to m^6A and in ssDNA to 6mA. m^6A marks are prevalent in eukaryotic mRNAs and lncRNAs and modulate their stability and fate in a context-dependent manner. The cytoplasmic METTL3 can act as a m^6A reader. However, the precise mechanism during m6A writing, reading, or sensing is unclear. Here, we present a ~2.5 Å structure of the methyltransferase core of human METTL3-METTL14 in complex with the reaction product mimic, N^6-methyladenosine monophosphate (m^6A), representing a state post-catalysis but before the release of m^6A. m^6A occupies an evolutionarily conserved RNA-binding pocket ~16 Å away from the SAM pocket that also frequently mutates in cancer. We propose a two-step model of *swiveling* of target A upon conversion to m^6A and *sensing* its methylation status by this pocket, enabling it to actuate enzymes' switch from writer to an m^6A-sensor. Cancer-associated mutations show impaired RNA binding dynamics, de-stacking, and defective m^6A writing and sensing.

Main

A heterodimer of Methyltransferase like-3 (METTL3) and its obligate partner METTL14 installs the majority of m^6A (N^6-methyladenosine) modification within the consensus DR$\underline{A}$CH (D=A/G/U, R=A/G, H=A/C/U) motif in eukaryotic mRNAs and lncRNAs[1-5], chromosome-associated regulatory RNAs (carRNAs)[6,7], and 7SK RNA[8]. METTL3 and METTL14 contain an MT-A70 family methyltransferase (MTase) core[9] diverged from an ancestral β-class of bacterial MTases[10-13]. METTL3 hydrolyzes SAM to facilitate the transfer of its methyl group to the N^6 amino group of the target adenine base in RNA *(in vivo* and *in vitro)*[1,4,9] and ssDNA *(in vitro)*[11,12]. In contrast, catalytically deficient METTL14 stabilizes METTL3 and is thought to position RNA in METTL3's active site[14-17]. m^6A modifications modulate RNA stability and play essential roles in myriad biological processes, including but not limited to miRNA biogenesis, maintenance of neural stem cells, translation efficiency, transcription elongation, innate immune response, DNA break repair, circadian rhythm, and viral pathogenesis[18,19]. Consistently, severe growth defects observed in the cellular KO phenotype of METTL3 underscore METTL3's essential role in maintaining cellular homeostasis during development[20-22], cancer growth[23-26], and viral infections, including SARS-CoV-2[27-29].

While m^6A deposition in mRNAs occurs in the nucleus and elevated METTL3 levels are associated with survival of acute myeloid leukemia[24,30], non-catalytic functions of METTL3 outside the nucleus benefit lung cancer cells[23,25]. Cytoplasmic METTL3 can act as an m^6A reader to promote the translation of mRNA of known oncogenes, thereby facilitating the crosstalk between m^6A-bound METTL3 at 3'-end to the translation initiation machinery that has engaged the 5'- mRNA cap[23,25,31].

62

m^{6}A marks are also present in genomes of RNA viruses such as hepatitis C, Zika, dengue, West

Nile, yellow fever, and SARS-CoV-2, and modulate viral replication and host immune response[27].

Thus, METTL3 has emerged as an attractive drug target for anti-cancer and anti-viral therapy

development. Consistently, pharmacologic inhibition of METTL3 limits the growth of acute

myeloid leukemia[26] and SARS-CoV-2[28,29]. The first METTL3 inhibitor STC-15 that targets its

SAM pocket has entered Phase I clinical trial (NCT05584111).

Despite significant advancement in the m^{6}A field and interest in targeting it for therapy, the

structural details of RNA recognition and catalysis by METTL3-METTL14 are lacking. Here we

present a ~2.5 Å crystal structure of the methyltransferase core of METTL3-METTL14 bound to

methyladenosine monophosphate (m^{6}A), a product mimic of the methylation reaction (Fig. 1a).

We show that m^{6}A occupies a novel cryptic pocket constituted to a large extent by residues from

METTL3 and an interface arginine (R298) of METTL14. This pocket is evolutionarily conserved

in mammals, plants, and yeast (Fig. 1b). Importantly, residues that partake in interaction with m^{6}A

are mutated in gynecologic, stomach, kidney, and bladder cancers[32] (Fig. 1b). When introduced

into wild-type METTL3-METTL14, the mutant enzymes exhibit a significant loss in catalysis,

perturbed RNA binding, and compromised ability of de-stacking of the target adenine for

presentation to the active site. Our data suggest that the target base swivels ~120º after methylation

for sensing by the cryptic pocket located ~16 Å away from the point of methyl transfer. METTL3-

METTL14 uses this unique mechanism to sense the methylation status before releasing the

substrate RNA. This arrangement will require de-stacking of the target base during catalysis and

sensing. We also show that the wild-type METTL3-METTL14, but not the mutant, binds more

85 tightly to an m^{6}A-modified RNA to distinguish it from the unmethylated RNA. Moreover, the

86 enzyme harboring R298P mutation, the most frequent mutation in endometrial cancer[32], exhibits

87 sub-optimal RNA binding, catalysis, and base de-stacking ability. Our results uncover entirely

88 unexpected operating principles underlying methyl transfer and m^{6}A-sensing by METTL3-

89 METTL14.

90

91 **Results and Discussion**

92 **Overall structure**

93 The MTase cores of human METTL3 (aa 358 - 580) and METTL14 (aa 116 - 378) form an obligate

94 heterodimer. METTL3 acts as an active SAM-dependent MTase, whereas METTL14, an inactive

95 MTase, stabilizes RNA[14-17]. We co-purified the MTase core of METTL3-METTL14 from *E. coli.*

96 We succeeded in resolving its structure in the presence of *N^6*-methyladenosine 5'-monophosphate

97 (m^{6}AMP, referred to as m^{6}A), a product of methylation reaction, by soaking m^{6}A into apo crystals

98 (Fig. 1 a, Extended data Fig. 1a-c). The difference omit map showed clear and unbiased electron

99 density for m^{6}A, which was refined well with no discrepancies for the ligand, surrounding regions,

100 or the rest of the protein (Extended data Fig. 1d-g and table 1). METTL3-METTL14-m^{6}A model

101 was refined to ~2.5 Å resolution, with excellent stereochemistry and R$_{free}$ and R$_{work}$ of ~26.2 and

102 22.9%, respectively (Extended data Table 1). The final model contains one molecule each of

103 METTL3 (aa 369 – 579), METTL14 (aa 116 – 402), one m^{6}A, 90 water, and two ethylene glycol.

104

105 The overall fold of METTL3-METTL14 is similar to those reported previously[14-16], except for

106 notable changes in the region around the m^{6}A binding pocket. MTases adopt a β-class of MTase

107 fold with a central β-sheet of seven parallel and one antiparallel β-strands flanked by three helices

108   on each side. Three major loops (gate loops 1 and 2 and an interface loop) emanating from the

109   central β-sheet of METTL3 participate in SAM, RNA, and METTL14 binding. While the two gate

110   loops exhibit high flexibility upon SAM or SAH binding and release, the interface loop remains

111   rigid due to extensive protein-protein contacts from METTL14 MTase (Fig. 1a).

112

113   While the MTase core of METTL3-METTL14 is not catalytically active form, its structures

114   derived by soaking SAM or SAH into these crystals provided crucial insights into the binding of

115   methyl donor (SAM) and byproduct (SAH) and important conformational changes in the regions

116   of METTL3 (gate loops 1, 2) surrounding these ligands[14-16]. The m6A-bound structure, which we

117   report here, is the first nucleotide-bound form of the MTase core of METTL3-14 and provides

118   crucial insights into the mechanism of this critical enzyme that is central to normal homeostasis

119   and diseases. Since a small molecule targeting the catalytic pocket of METTL3 has entered human

120   clinical trials for cancer therapy, our results showing the nucleotide binding in the regions outside

121   of catalytic and SAM-binding pockets will pave the way for the rational design of more specific

122   inhibitors.

123

124   **Evolutionarily conserved m^{6}A pocket plays an essential role in m^{6}A sensing**

125   Strikingly, m^{6}A occupies a cryptic pocket ~16 Å away from the methyl donor SAM pocket with

126   its *N^6*-methyl moiety in an energetically favored *syn* conformation, facing outward (Fig. 1a).

127   Previously, this region was postulated to bind RNA due to its positive charge and polar nature[14-16].

128   m^{6}A is stabilized by a vast network of specific interactions, mostly from METTL3 and R298 of

129   METTL14. The purine ring of m^{6}A is sandwiched between the side chain of M402 and the

130   backbone atoms of the interface loop residues, R471, T472, G473, and H474. The two arginine

131   residues (R471 of METTL3 and R298 of METTL14) act like a *clasp* to hold the N^6-methyl moiety

132   in place through a direct h-bond between R298 and N^1, van der Waals and hydrophobic interactions

133   between N^6-methyl and its aliphatic portion, and the amino group of the R471 side chain,

134   respectively. The carbonyl oxygen of G473 appears to neutralize the positive charge of the R298

135   residue. The carbonyl moiety of R471 embraces the N^6 atom of m^{6}A via a direct h-bond, while the

136   opposite side is stabilized by the side chain of H474 via a π-π interaction. Altogether, the *arginine*

137   *clasp*, interface loop residues R471-H474 and M402, forms a partial closure around the methylated

138   purine ring of m^{6}A. The ribose in the C3'-endo conformation is stacked between the backbone

139   atoms of G473 and H478 and the side chains of I400 and H478. The phosphate group of m^{6}A is

140   locked in place by multiple direct h-bonds with its phosphoryl oxygens and side chains of H478,

141   E481, T433, and K459 (water-mediated) – all from METTL3, and another water-mediated

142   interaction with E257 of METTL14. The side chain of H478 holds the m^{6}A phosphate on one side

143   and E257 of METTL14 on the other, thus acting as a hinge (Fig 1a, Extended data Fig. 1g).

144   Strict conservation of the extensive interaction network of m^{6}A in human, animal, plant, and yeast

145   suggests that m^{6}A sensing by this cryptic pocket is an evolutionarily conserved mechanism (Fig.

146   1b). Several key residues that partake in m^{6}A binding, such as R471 and R298 of the *arginine*

147   *clasp*, E481, and H478 that stabilize the N^6-methyl and phosphate groups are recurrently mutated

148   in endometrioid and adenocarcinoma[32] (Fig. 1b). We introduced the R298P mutation in METTL14,

149   a recurrent mutation event in endometrioid carcinoma[32,33], and the R471H, E481A, T433A,

150   K459A, and H478A mutations in METTL3. In addition, we generated two deletion mutants (Δ472-

151   473, Δ472-474) in which three residues of METTL3 (T472, G473, H474) that stack against the

152   purine ring of m^{6}A were deleted to shorten the interface loop.

153

154   We co-purified the full-length wild-type human METTL3-METTL14 and eight mutant enzymes

155   from insect cells and probed their RNA methylation and binding activities. We used a 30-mer RNA

156   oligo (NEAT2*) consisting of one canonical GG$\underline{A}$CU motif. Consistently, R298P and R471H

157   mutants significantly reduced (up to 85%), whereas T433A resulted in ~20% loss in

158   methyltransferase activity, agreeing with the reduced m^{6}A levels observed in endometrial tumors

159   harboring the R298P mutation[33]. The other five mutations in METTL3 (Δ472-473, Δ472-474,

160   K459A, E481A, and H478A) completely abolished the RNA methyltransferase activity of

161   METTL3-METTL14 (Fig. 1c). Thus, the evolutionarily conserved m^{6}A binding pocket is essential

162   for efficient conversion of A to m^{6}A.

163

164   Next, we quantitatively determined the binding affinities of wild-type (WT) and mutant enzymes

165   to the substrate and a product RNA, wherein the target A base within GG$\underline{A}$CU is replaced by m^{6}A.

166   We covalently attached a fluoresceine moiety to the 5'-end of both the substrate NEAT2* (A-RNA)

167   and product (m^{6}A-RNA) RNAs and performed fluorescence polarization-based assays. The WT

168   enzyme can still bind the m^{6}A-RNA and A-RNA with high affinity (K_d = 9-20 nM) (Fig. 1 d,e),

169   corroborating previous studies attributing a sort of m^{6}A-reader function to METTL3 *in*

170   *vivo*[23,25,31,34]. In contrast, the mutants, including R298P and R471H (both mutated in cancers and

171   belong to the *arginine clasp* motif that stabilizes the m^{6}A) exhibited a loss in binding affinity with

172   varying degrees, with R298P showing weakest binding (Fig. 1e, Extended data Fig. 1h). Thus,

173   inability to sense and distinguish m^{6}A properly by the R298P mutation could result in total m6A

174   and promote tumorigenicity and growth of endometrial tumors as observed previously[33]. The

175   nanomolar affinity observed in this fluorescence polarization (FP)-based assay for mutant enzymes

176   suggests a significant contribution of accessory motifs such as zinc fingers (ZnFs) of METTL3

177   and RGG repeats of METTL14 to RNA binding, especially the predicted bulged stem-loop

178   structure of NEAT2* RNA (A-RNA). These motifs are intact in both the wild-type and the mutant

179   enzymes. This could be one of the reasons for not observing the radical change in overall RNA

180   binding as measured by the equilibrium dissociation constant (Kd) for A vs. m6A RNA in an FP-

181   based assay. Moreover, the residue aligning the catalytic and cryptic pockets would interact with

182   the substrate (A) and the product (m6A) nucleotide of the 'DR**A**CH' sequence during the pivoting

183   of the base upon conversion to m6A, respectively. Even if the mutations in the cryptic pocket retain

184   overall RNA binding dominated by domains flanking the MTase core (ZnFs and RGG) and the

185   secondary structure of RNA itself (GGACU containing stem-loop RNAs show higher affinity),

186   they could still influence the pivoting of the m6A base and its release after conversion.

187

188   We also performed a kinetic analysis by varying the concentration range of RNA substrate from

189   10 nM to 10 µM in the presence of a saturating concentration of SAM (10 µM) (Fig. 2a).

190   Consistently, these results show that the wild-type enzyme yields the highest methylation activity,

191   whereas the mutant enzymes show reduced methylation. Next, we studied the binding kinetics of

192   the full-length METTL3-METTL14, wild-type (WT), and the two mutant enzymes harboring

193   R298P and R471H mutations in METTL14 and METTL3, respectively. We employed the surface

194   plasmon resonance (SPR) technique, a gold standard for studying binding kinetics that includes

195   ON (K_{on}) and OFF (K_{off}) rates of RNA binding. We used our original RNA substrate, NEAT2 (30-

196   mer bulged stem-loop) RNA, and its methylated version (NEAT2-m6A). We also examined a 14-

197   mer linear RNA substrate (r6T) and its methylated form (r6T-m6A) to fully understand the kinetics

198   of enzyme binding to GGACU-containing RNAs with different shapes and sequences. The SPR

199   data of the WT enzyme fit well with a 1:1 binding model. As shown in Fig. 2b and Tables 1-3, the

200   binding affinity and kinetics of METTL3-METTL14 enzymes differ significantly on the two RNA

201   oligos tested. The structured NEAT2 RNA shows a 5-fold tighter affinity than a linear r6T

202   substrate, while their methylated counterparts show reduced binding (1.3-fold for NEAT2-m6A

203   and 2.3-fold for r6T-m6A), but the Kds (dissociation constants) are still in sub and low-micromolar

204   range.

205

206   Interestingly, the ON (K_{on}) and OFF (K_{off}) rates for a linear substrate RNA differ 2-2.7-fold

207   compared to NEAT2 RNA. A 2.7-fold faster OFF rate on a linear substrate would result in a rapid

208   turnover and higher methylation of the GGACU motif residing in a linear RNA compared to the

209   loop region of a stem-loop RNA. At the same time, the structured elements in RNA can help recruit

210   METTL3-METTL14, as suggested by a 5-fold stronger affinity to NEAT2 RNA. These results

211   suggest the RNA shape surrounding the core 'GGACU or DRACH' motif is a crucial determinant

212   of methylation. This observation can explain, in part, why only a fraction of potential DRACH

213   motifs (or perfect GGACU) are methylated *in vivo*.

214

215   The SPR data of the two mutant enzymes (R471H and R298P) revealed a change in Rmax and

216   mode of binding. While the SPR data of the WT enzyme fit well with the 1:1 binding model, the

217   mutant data could only fit well with a two-state reaction model (Table 3). The R298P mutation in

218   METTL14 results in a moderate loss (1.4-1.6-fold) of binding to the stem-loop NEAT2* RNA

219   (Kd=256 vs. 356 nM) and its methylated counterpart (Kd= 337 vs. 538 nM) or the linear r6T RNA

220   (Kd=1360 vs. 2160 nM) but a significant loss (>7-fold) in RNA binding occurred for methylated

221   linear r6T RNA (Kd=3120 vs 22900). On the other hand, the R471H mutant exhibits much slower

222   dissociation after binding, thus hampering the enzyme's turnover. These data suggest that the two

223   arginines (R471H of METTL3 and R298P of METTL14) in the m6A pocket, which is cryptic in

224   nature, are important for recognizing the methylation status, and the replacement of R298 to

225   proline and R471 to histidine would negatively impact the methylation of the canonical GGACU

226   motif. Of note, striking differences in the mode of binding – two-state binding for R471H/ R298P

227   mutants vs. one-state binding of the WT enzyme – and their dynamics (ON and OFF rates) likely

228   alter the retention time of the enzyme on RNA with varied shapes and sequences or residence time

229   for m6A of these RNAs in the cryptic pocket. Consequently, multi-stage RNA binding and altered

230   dynamics could alter specificity. An independent study by Zhang et al. reported that R298P

231   mutation alters the enzyme's preference from GG<u>AC</u> to GG<u>AU</u>[35]. In this context, our structural

232   and binding data provides crucial and timely insights into the existence of a cryptic pocket, the

233   importance of two arginines for methylation of the canonical GGACU motifs, and how mutations

234   at these positions could alter the dynamics of RNA binding of METTL3-METTL14 and ultimately

235   alter enzyme specificity.

236

237   To assess the dynamic impact of the mutations in METTL3-METTL14 on m^{6}A binding, we

238   conducted supervised molecular dynamics simulations (SuMD) and analyzed the distances

239   between the center of mass (com) of the m^{6}A and the product m^{6}A binding pocket (defined by

240   residues within 4 Å of m^{6}A (see methods) over time for wild-type and each mutant, including

241   T433A, K459A, R471H, Δ472-473, Δ472-474, H478A, E481A, and R298P. The wild-type

242   METTL3-METTL14 complex displayed distances around 1.5 Å for most of the simulation time,

243   highlighting the presence of m6A within the product m6A binding pocket (Extended data Fig. 3a

244   and 4a). Furthermore, this also indicates that the product m^{6}A binding pocket in the wild-type is

245   well-structured to accommodate m^{6}A securely and thereby maintain a stable binding environment

246   (Extended data Fig. 3b). In the wild-type, interactions between H478, T472, and m^6A are observed.

247   Some additional interactions are also formed; for example, T433 and E481 form stable interactions

248   with the phosphate group via a water molecule. A salt bridge between K459 and E481 helps to

249   stabilize the water molecule (Extended data Fig. 4a). In H478A, which is no longer able to interact

250   with m^6A, the phosphate group becomes mobile and is unable to anchor to A478 (Extended data

251   Fig. 4f) . In T433A and R298P mutations, the distance between the center of mass of m^6A and the

252   product m^6A binding pocket mostly ranged from 2 to 4 Å, suggesting that these mutations, while

253   impactful, do not entirely abolish m^6A binding (Extended data Fig. 4b, c). Consequently, these

254   mutants could retain m^6A in the product m^6A binding pocket for most of the simulation time. It is

255   interesting to note that in the T433A mutation, in spite of the h-bond interaction between the

256   phosphate group and the side chain of T433 is lost, the interaction between H478 and the phosphate

257   group remains intact (Extended data Fig. 4c). Therefore, this T433A mutation does not

258   significantly affect the binding of m^6A. In the case of R298P (Extended data Fig. 4b), although the

259   *arginine clasp* was broken, the phosphate group remains stabilized in the same position, making

260   interactions with H478. Moreover, E481 in the R289P mutant can also contribute to stabilizing the

261   phosphate group via a water molecule (Extended data Fig. 4b). However, in the E481A mutant,

262   this water bridge is lost. Similarly, the mutation in K459A results in the loss of a salt bridge with

263   E481, leading to localized destabilization (Extended data Fig. 4d, g). The resulting electrostatic

264   repulsion between the negatively charged side chains of E481 and the phosphate group of m^6A

265   pushes the m^6A out of the product m^6A binding pocket (Extended data Fig. 4g). For the two

266   deletion mutants (Δ472-473, Δ472-474), m^6A immediately leaves the product m^6A binding pocket

267   after the removal of the constraint in the equilibration steps, highlighting the essential nature of

268   these residues in maintaining the binding pocket's structure (Extended data Fig. 4h, i).

269

Base swiveling facilitates m^{6}A sensing

271   The two loops in METTL3 (gate loops 1 and 2) surrounding the methyl donor SAM and acceptor

272   base A pockets show varying degrees of flexibility upon SAM and SAH binding from their original

273   positions in a ligand-free (apo) form[14-16]. Thus, we compared the m^{6}A structure with three states

274   (SAM, SAH, and apo). These loops also move in opposite directions upon m^{6}A binding from their

275   original positions in the SAM-bound METTL3 (Fig. 3a). Gate loop 1 (aa 398-409) moves ~ 5.7Å

276   inward to the direction of m^{6}A, whereas the gate loop 2 (aa 506-512) moves ~ 7.8Å outward, with

277   several residues in this region, including H512, that flips ~180°. The invariant T433 and G434

278   from a small loop between β3 and α2 move ~ 2.1Å with the side chain of T433 rotating ~90° to

279   stabilize the phosphate and ribose of m^{6}A (Fig. 3a). This region remains unperturbed in SAH-

280   bound METTL3, suggesting the m^{6}A binding to this pocket occurs after hydrolysis of SAM (Fig.

281   3b). While the gate loop 2 in SAH remains in open confirmation, akin to SAM conformation, the

282   position of gate loop 1 in m^{6}A experiences significant repositioning of the M402 side chain (Fig

283   3c). Although m^{6}A-bound METTL3 is most similar to the apo form with the smallest root mean

284   square deviation for superposition of 1539 atoms of METTL3 achieved for apo (1.2), compared to

285   SAH (1.5), and SAM (1.9), we observed notable changes in the m^{6}A pocket (Fig. 3c).

286

287   The side chain of M402 from gate loop 1 in the m^{6}A structure stacks over the purine ring of m^{6}A.

288   In the SAM-bound form, this region is moved >5Å away, but in the SAH and apo forms, the M402

289   side chain will sterically clash with m^{6}A ribose (distance between Cε of M402 and C4' of ribose

290   ~1.2 Å). To avoid this clash, the side chain of M402 in m^{6}A-METTL3 rotates > 45°, resulting in a

291   ~3.8Å gain in the distance for the Cε atom compared to its position in the apo structure. As a result

292 of this repositioning, the inter-gate area between interface loop (H474) and gate loop 1 (M402)

293 becomes wider, from 6.8Å in apo to 8.0 Å in the m^{6}A structure (Fig. 3d). Thus, gate loop 1 from

294 one side senses the SAM and targets the RNA base at the point of catalysis (^{395}DPPW^{398} motif). It

295 then swivels after SAM hydrolysis to facilitate the sensing of m^{6}A status of the target base at the

296 opposite or *exit* site.

297

298 Another change occurs in how the side chain of invariant R298 (METTL14) orients within the

299 *arginine clasp*. The R298 side chain rotates ~180º around its C$_\beta$, although the guanidino group

300 shifts slightly to form a direct h-bond with N^1 of m^{6}A (Fig. 3d, Extended data Fig. 1g). The

301 orientation of the gate loops suggests that m^{6}A-METTL3 represents a state of enzyme post-

302 catalysis before release of any product or enzyme reset.

303

304 How does m^{6}A swivel ~16Å from the point of catalysis to occupy this novel pocket in METTL3?

305 To answer this question regarding the mechanism of base-swiveling, we once again employed

306 supervised molecular dynamics (SuMD) simulations. The simulations successfully captured the

307 transition of the m^{6}A from the substrate A pocket to the product m^{6}A binding pocket. The

308 phosphate group of m^{6}A makes h-bond interactions with H478 (Extended data Fig. 4a). This

309 interaction acts like a hinge and anchors m^{6}A, which then allows the nucleotide base in m^{6}A to

310 swivel and eventually occupy the product m^{6}A binding pocket. Once in the product m^{6}A binding

311 pocket, the nucleotide base of m^{6}A can form h-bond with R298 (Extended data Fig. 4a). The most

312 stable structure of the m^{6}A in the product m^{6}A binding pocket displays a root-mean-square

313 deviation (RMSD) of ~ 2 Å with the resolved crystal structure (Extended data Fig. 5). This close

314 structural alignment with the crystallographic data highlights the significance of the observed

315 transition mechanism and corroborates with the H478A mutation where the RNA

316 methyltransferase activity is completely abolished in the METTL3-METTL14 complex. To further

317 validate these interactions, we calculated the interaction energy between m^{6}A and the METTL3-

318 METTL14 complex (Extended data Fig. 5-7). The results showed significant binding affinity and

319 stability, supporting the observed h-bond interactions and the overall structural integrity of m^{6}A

320 within the m^{6}A binding pocket (Extended data Fig. 7).

321

322 To verify our findings, we superposed m^{6}A-METTL3 over the structure of Arabidopsis METTL4,

323 a member of the subclade of the MTA-70 family that possesses the substrate 2'-*O* methyladenosine

324 (A$_m$)[36]. The central β-sheet and the catalytic motif of the two enzymes (DPPW) overlay very

325 closely. In this model, the acceptor *N^6* atom of Am resides at ~3Å or less from the methylsulfonium

326 group of SAM for S$_N$2 mechanism of direct methyl transfer. The phosphates of A$_m$ and m^{6}A lie in

327 close proximity (~1.2Å). However, their purine and ribose rings are rotated ~120º in opposite

328 directions, suggesting the base (A) pivots after conversion into m^{6}A (Fig. 3e). Such a rotation may

329 necessitate the de-stacking of the target base for its presentation to catalytic pocket and or base

330 swiveling.

331

332 A water molecule at the putative site of the substrate A base is present in the m^{6}A structure to

333 compensate for the loss in binding energy in the emptied site by rotation of m^{6}A from this site

334 post-catalysis. This water coordinates with K459, and its mutation to alanine abolishes the

335 methylation activity (Fig. 1c). SAM-dependent DNA methyltransferases, including the ancestral

336 members of MTA-70 family MTases such as EcoP15I, efficiently flip the target adenine base out

337 of the DNA helix into the catalytic pocket[37]. Although METTL3-METTL14 does not methylate

338   dsDNA and dsRNA[11,12], it can still de-stack the target base from a single-stranded RNA into the

339   catalytic pocket, similar to the m^6A/m^6A_m eraser enzyme, FTO[38,39], and the m^6A reader,

340   YTHDC1[40]. To test this activity, we replaced the target A (6-aminopurine) in a GG<u>A</u>CU in a 14-

341   mer ssRNA with 2-aminopurine (2Ap), a fluorescent nucleobase used as a conformational probe

342   due to its high sensitivity to changes in the local environment induced by DNA[41] and RNA

343   MTases[42]. As shown in Fig. 3f, the change in fluorescence intensity (at 371nm) with increasing

344   enzyme concentrations was rapid for WT but not the R298P mutant enzyme, confirming the

345   diminished RNA binding and base de-stacking ability of the mutant enzyme. While the cellular

346   impact of R298P mutation has been studied in the context of cancer[33], our data now uncover a

347   precise mechanistic role of R298 in m^6A sensing. Thus, an elegant orchestration of loops

348   surrounding the SAM/SAH, substrate A, and product m^6A binding pockets enables m^6A base

349   swiveling and sensing (see Movie 1).

350

351   To capture an AMP-bound METTL3-14, which could serve as a control structure, we extensively

352   attempted co-crystallization and soaking of AMP into apo crystals but could not observe AMP

353   around the catalytic pocket (DPPW or motif IV) or the m6A binding pocket. We reason the highly

354   mobile nature of the substrate adenine base in the catalytic pocket for this. To gain insights into

355   this phenomenon, we examined the Am binding of the published structure of Arabidopsis METTL4

356   (PDB: 7CV6)[36]. The slightly low occupancy coupled with high average B-factors (B = 177 $Å^2$) of

357   Am base in Arabidopsis METTL4 suggest a highly mobile nature of the Am base in the catalytic

358   pocket (Extended data Fig. 2a). Furthermore, Am's RSCC (real space correlation coefficient) score

359   in Arabidopsis METTL4 is 0.66. A value of RSCC score below 0.8 indicates a modest fit[43]. In

360   contrast, the m6AMP in our hMETTL3-METTL14 methyltransferase core structure fits nicely into

361   the electron density at full occupancy (1.0) (Extended data Fig. 1 d-f). Consistently, an RSCC score

362   of 0.85 with low average B-factors (B = 70 Å^2) confirms a relatively stable mode of m6A binding

363   to hMETTL3-METTL14 (Extended data Table 1 and PDB validation report).

364

365   While our work was in preparation, Corbeski et al. reported crystal structures of METTL3-

366   METTL14 MTase core in complex with synthetic bisubstrate analogs (BAs), wherein methyl

367   donor SAM was covalently linked to the substrate adenosine. These analogs may represent a

368   transition state during methyl transfer[44]. This study suggests that the substrate nucleotide-bound

369   structures of METTL3-METTL14 could only be resolved when the N^6 of adenosine was covalently

370   attached to SAM via a 2-3 carbon linker. Interestingly, despite spatial restriction imposed by

371   covalent linkage, the substrate adenosine moiety still exhibits significant flexibility within and

372   across crystals obtained from soaking two different analogs, e.g., BA2 and BA4 (Extended data

373   Fig. 2b, c). For example, the adenosine moiety of the covalent analog BA2 samples two different

374   orientations; in a 'buried' conformation, it occupies the substrate pocket of METTL3 and interacts

375   with E481 and K513, whereas in an 'alternate conformation,' it rotates ~90º and exposes to the

376   solvent. In the BA4-METTL3-14 structure, the covalently attached substrate adenosine rotates into

377   solvent-exposed orientation while the cosubstrate SAM remains rigid and occupies the SAM-

378   binding pocket in both structures (Extended data Fig. 2b, c). Importantly, the movement of the

379   adenosine in BA-analogs will be limited due to the covalent linkage to SAM, which naturally has

380   a high affinity. However, the adenosine continuously tries to move in and out of the catalytic

381   pocket. We believe these structures could serve as a control where adenosine is captured in the

382   methyl acceptor state of the N^6, precisely the way we modeled it by comparing the METTL4-Am

383   structure.   Moreover, the gate loop 1 and the interface loop are disordered in METTL3-14

384 bisubstrate analog structures, most likely due to the lack of stabilizing interactions. In contrast,

385 these regions of METTL3-14 are well resolved in our m6AMP-bound structure due to their

386 stabilizing interaction with m6AMP. Altogether, these observations suggest a highly mobile nature

387 of the substrate adenine (A) base in the catalytic pocket.

388

389 The center of mass distance measurements in the simulations revealed that m^{6}A consistently

390 maintained the shortest average distance of ~1.5 Å with low variability, indicating a strong and

391 persistent binding interaction. In contrast, other nucleotides exhibited greater and more variable

392 distances, typically exceeding 2 Å and occasionally reaching up to 5 Å, especially AMP, CMP, and

393 GMP, suggesting weaker and less stable interactions. AMP, CMP, and GMP showed the largest

394 RMSD values, > 4 Å, indicating the least stability in their binding positions (Extended data Fig.

395 3b). This instability can be attributed to the inability of M402 to form hydrophobic interactions

396 with the methyl group of m6A. In AMP, the loss of the methyl group prevents M402 from

397 stabilizing the nucleotide. Although AMP can still form strong interactions with the complex, the

398 RMSD plot indicates significant flexibility within the binding pocket. The results from SuMD are

399 in excellent agreement with our experimental findings, which highlight the specific binding

400 preference of the METTL3-METTL14-core for m^{6}A.

401

402 **METTL3-METTL14 acts as an atypical m^{6}A sensor**

403 The m^{6}A-METTL3-METTL14 structure allowed us to gain valuable insights into how m^{6}A writer

404 (METTL3-METTL14), eraser (FTO), and reader (YTHDC1) proteins accommodate m^{6}A. We

405 examined their m^{6}A pocket in detail (Fig. 4a-c). Despite the lack of obvious resemblance at the

406 protein sequence, domain, and structure levels, we observed high similarity in the interaction

407   networks of m^{6}A in METTL3-METTL14 to the binding mode of 6mA in FTO (PDB: 5ZMD) and

408   m^{6}A in YTHDC1 (PDB: 4R3I) (Fig. 4). Of note, the purine ring of 6mA in FTO stacks between a

409   hydrophobic amino acid, L109 (the equivalent of M402 in m^{6}A), from the top and the backbone

410   atoms of V228, S229, and H231 (the equivalent of T472, G473, and H474 in m^{6}A) from the

411   bottom. Interestingly, the *arginine clasp* we found in m^{6}A-METTL3-METTL14 is also present in

412   6mA-FTO. Notably, the side chain of R96 in FTO forms a direct h-bond to N^1 of 6mA, while the

413   guanidino group of its R322 residue forms a van der Waals interaction with N^6 methyl group, akin

414   to identical interactions by R298 and R471 to stabilize m^{6}A in m^{6}A-METTL3-METTL14. Stacking

415   interactions that lock the sugar moieties in place also display similarities. For example, the sugar

416   of 6mA in FTO stacks between I85 and H231, whereas the sugar of m^{6}A stacks between I400 and

417   H478 of METTL3 (Fig. 4a, b).

418

419   We found that m^{6}A in METTL3-14 and YTHDC1 (PDB: 4R3I) had many similarities and striking

420   differences, mainly in the orientation of the base (Fig. 4c). The N^1 of m^{6}A forms an h-bond with

421   N367, whereas an h-bond with carbonyl of S378 akin to carbonyl of R471 of METTL3 stabilizes

422   the N^6. Additional hydrophobic interactions from W377 and W428 also support the N^6 methyl

423   group in YTHDC1. The nature of stacking interactions for the purine ring is also similar, i.e.,

424   hydrophobic residues M434, L380, and L439 on one side and backbone atoms of K361, S362, and

425   N363 on the other. However, the orientation of the m^{6}A base in YTHDC1 is reversed by 180º

426   compared to 6mA in FTO and m^{6}A in METTL3-14. As such, when the direction of sugars and

427   phosphates of modified bases is aligned in three structures (facing downward in Fig. 4a, b, and

428   upper panel of c), the hydrophobic residues (M434/L380/L439) in YTHDC1 stack from the bottom

429   side and the backbone atoms of K361, S362, and N363 stack from the top side, in contrast to the

430   base orientation in FTO and METTL3. A ~180º rotation of YTHDC1 will place the interacting

431   residues in all three proteins in the same plane. However, the orientation of ribose and phosphate

432   of m^{6}A in YTHDC1 will also be reversed (facing upward, Fig. 4c lower panel). Thus, a m^{6}A reader

433   protein approaches the m^{6}A entirely differently than a writer or eraser. This unique geometric

434   difference may allow the reader to avoid clashes with a writer or eraser enzyme acting

435   simultaneously on the same transcript.

436

437   There could be two scenarios for stabilizing m6A in the cryptic pocket: **a.** The pocket may have

438   the capacity to bind to all nucleotides, but m6A can outcompete other nucleotides due to its higher

439   binding affinity to the MTase core. **b**. The pocket may exclusively interact with m6A while

440   nucleotides flanking A/m6A weakly interact with other RNA binding domains of METTL3-14.

441   Consequently, mutations near the pocket could disrupt the binding to m6A or alter the preference

442   from m6A to other nucleotides. We show that METTL3 possesses features that enable it to act as

443   an atypical m^{6}A sensor/reader – a function ideally suited for its emerging non-catalytic functions,

444   including crosstalk with eIF3H to promote mRNA circularization, thereby enhancing RNA

445   translation as observed in lung cancer[23,25] and bone marrow mesenchymal stem cells[21].

446   Consistently, METTL3 exhibits a strong affinity to a methylated (m^{6}A) RNA form, especially

447   those containing secondary structures, a feature that could be important for its non-catalytic roles

448   such as an 'm^{6}A reader' for an alternative mode of translation initiation during oncogenic

449   translation[23,25] and cellular stress (e.g., heat shock)[34].

450

Methods

METTL3-METTL14 MTase core

The gene encoding the MTase domains of human METTL3 (aa 357-580aa) and METTL14 (aa 116-402) were cloned into a pETduet-1 vector and expressed in E. coli NiCo21(DE3) cells. The transformed cells were grown in Terrific Broth medium supplemented with 1 mM ampicillin at 37°C until OD$_{600nm}$ reached 0.6. Protein expression was then induced by adding 0.4 mM isopropyl β-D-thiogalactopyranoside, and the culture was grown at 18°C for 16 hrs. The cell pellets were harvested by centrifugation at 6000 r.p.m. at 4°C and resuspended in cold lysis buffer containing 25 mM Tris pH 8.0, 0.5 M NaCl, 10% glycerol, 5 mM imidazole, 0.1 mM TCEP, one tablet of protease inhibitor (Roche), lysozyme (0.1 mg/mL), and DNase I (5U/mL) and stirred gently at 4°C until achieving full homogeneity. Resuspended cells were lysed by two passages through a microfluidizer (Analytik, UK) and subjected to centrifugation at 41,000 r.p.m. for 50 min at 4°C. The clarified supernatant was filtered through a 0.22 μm filter and loaded onto a Nuvia IMAC column (Bio-Rad) pre-equilibrated with wash buffer (25 mM Tris pH 8.0, 0.5mM NaCl, 10% glycerol, 5 mM imidazole, and 0.1 mM TCEP). The His-tagged METTL3 was co-eluted with untagged METTL14 by increasing the imidazole concentration. The eluates were dialyzed in a buffer lacking imidazole overnight at 4ºC in the presence of the ULP1 enzyme to remove the His-SUMO tag from METTL3 proteolytically. The dialyzed proteins were then re-loaded onto an IMAC column to remove un-cleaved proteins and the His-SUMO tag. Two successive passages through MonoQ and Hiload Superdex75 columns (Cytiva) further purified the tag-free complex. The fractions of a homogenous peak eluted in 20 mM Tris pH 8.0, 0.2 M NaCl, and 0.1mM TCEP were pooled, concentrated to 15 mg/ml, and either used immediately or flash-frozen in liquid nitrogen and then stored at -80°C.

Full-length METTL3-METTL14 and mutants

The full-length human METTL3 and METTL14 (wild-type and mutants) were expressed in insect cells (ExpiSF Expression System, Thermo Fisher) and purified using a protocol published earlier[12]. In brief, the METTL3 and METTL14 plasmids were transformed individually into Max Efficiency DH10Bac competent cells (Thermo Fisher) to generate the DNA bacmids. The successful insertion of genes was confirmed by PCR amplification using a pUC/M13 primer (Forward: 5'-CCCAGTCACGTTGTAAAACG -3', Reverse: 5' – AGCGGATAACAATTTCACACAGG -3'). The amounts of purified bacmids and ExpiFectamine SF transfection reagent (Thermo Fisher) were optimized as per the manufacturer's recommendations (Thermo Fisher). The ExpiSf9 insect cells were cultured in ExpiCD medium (Thermo Fisher) at 125 r.p.m. and 27°C in a non-humidified, air-regulated environment. The cells were harvested 72 hrs post-infection by spinning at $300 \times g$ for 5 min. The PBS-washed cells were resuspended in cold lysis buffer containing 0.5% Igepal, two tablets of protease inhibitor (Roche), and DNase I. Cells were lysed by passing through a microfluidizer (Analytick, UK) and clarified by centrifugation at 41,000 r.p.m. for 40 min.

The proteins were purified using a strategy similar to that of the MTase core, except for removing the His-tag from METTL3. This step was achieved by incubating proteins after the affinity column step with TEV protease for 3 hrs at room temperature. A second passage through a nickel IMAC column removed contaminants and any uncleaved fractions. The complex was then successfully purified by successive passages through HiTrap Heparin and Hiload Superdex 200 columns (Cytiva). Eluates from a homogenous peak of a Superdex column run in a buffer of 0.02 M Tris pH 8.0, 0.15 M NaCl, and 5% glycerol were pooled, concentrated to 1-3 mg/ml, and flash-frozen in liquid nitrogen and stored at -80°C. All full-length METTL3-METTL14 mutants (METTL3:

498   T433A, K459A, R471H, Δ472-473; Δ472-474, H478A, E481A; METTL14: R298P) were

499   generated by site-directed mutagenesis and purified by the same method as the wild-type protein.

500

501   Crystallization, data collection, and structure determination

502   The crystallization of the human METTL3-METTL14 MTase core (at 10 mg/mL concentration)

503   was carried out by an OryxNano robotic system (Douglas Instruments) using the sitting-drop vapor

504   diffusion method at 20°C. Initial crystals were grown in a solution containing 0.1 M MES pH 6.0,

505   1.0 M potassium sodium tartrate. After several rounds of optimization by varying pH and salt

506   concentrations, large reproducible crystals were grown in seven days. The N^6-methyladenosine

507   monophosphate (m^{6}AMP; Sigma, M2780) was soaked into native crystals (2.0 mM concentration)

508   for 1 hr at 20°C. A complete diffraction dataset was measured to ~2.5Å at GMCAT 23ID-D

509   beamline at Advanced Photon Source, Chicago, IL. The apo structure of METTL3-METTL14

510   MTase core (PDB: 5IL0) was used as a search model for molecular replacement in Phenix[45]. The

511   structure was iteratively built and refined using Coot (Version 0.9.8.6)[46], Phenix (Version 1.15.2-

512   3472) and Buster (Version 2.10.4)[47], respectively. The ligand geometry restraints were generated

513   by Grade. All structure figures were generated using Pymol (Schrodinger Suite).

514

515   *In vitro* methyltransferase assays

516   5 μM [methyl-^{3}H] SAM (PerkinElmer), 10 μM substrate RNA (NEAT2*: 5' –

517   GCCUAGUAGCAGAGA<u>GGACU</u>GCUCCUUGGU - 3'), and 2 μM purified WT or mutated

518   METTL3-METTL14 were mixed and incubated at 37°C for 1 hr in a total volume of 5 μL in a

519   reaction buffer (50 mM HEPES pH 7.5, 5 mM NaCl, and 1 mM DTT). The reactions were

520   quenched by blotting 3 μL of each on the Hybond-N+ membrane (Amersham). The methylated

521   substrates were then crosslinked by exposing them to ultraviolet light (254 nm) for 2 min. The

522   membranes were washed three times with 1X PBS, followed by two 95% ethanol washes. Then

523   the membranes were air-dried inside the hood for 15 minutes, and the RNA probe's count per

524   minute (c.p.m.) on each membrane were measured by a scintillation counter (Beckman LS6500).

525   All results are reported as the means from three independent experiments (n=3) for each group,

526   with one standard deviation (s.d.).

527

528   Fluorescence polarization

529   The reactions were carried out in a buffer containing 10 mM HEPES pH 7.5 and 50 mM KCl. The

530   two 30-mer RNA probes (native RNA or A-RNA and its m^6A-modified version or m^6A-RNA)

531   were synthesized with a fluresceine moiety covalently attached to their 5'-end, de-protected, and

532   purified using HPLC (HorizonDiscovery). The sequence of A-RNA was identical except the target

533   A base within the characteristic motif (underlined and bold) in native A-RNA (Fl-NEAT2*: 5' –

534   [Fl]GCCUAGUAGCAGAGA<u>**GGAC**U</u>GCUCCUUGGU - 3'), was replaced by N^6-

535   methyladenosine (m^6A) in the modified RNA (Fl-NEAT2*-m^6A: 5' –

536   [Fl]GCCUAGUAGCAGAGA<u>**GG[m⁶A]**C</u>GCUCCUUGGU - 3'). A constant 5 nM of RNA

537   probes were incubated with increasing concentrations of the purified WT or mutant METTL3-

538   METTL14 enzymes in a 384-well plate. The fluorescence polarization values (excitation

539   wavelength = 485 nm, emission wavelength = 530 nm) of each reaction were measured by

540   PHERAstar FS (BMG Labtech). The affinity of RNA-protein binding was calculated by a simple

541   one-site specific binding model (Y = Bmax*X/(Kd+X), X = protein concentration, Y = specific

542   binding, Bmax = maximum specific binding, Kd = equilibrium dissociation constant). The results

543   were analyzed and fitted by GraphPad Prism (GraphPad Software, San Diego, CA). Each

544   experiment was repeated three times independently (n=3), and final K_d is reported as the mean of

545   the three replicates with standard deviation (s.d.) for each RNA shown as error bars.

546

547   Steady-state fluorescence assays

548   For this experiment, we used a 14-mer single-stranded RNA probe in which the the target adenine

549   base within the m^6A motif was replaced with 2-aminopurine (2-Ap) (r6T*: 5' – CUUC<u>GG[2-</u>

550   <u>Ap]CU</u>CUGCU – 3'). In a 384-well plate format, 0.5 µM of RNA probe mixed with increasing

551   concentrations (1 – 5 µM) of full-length human WT or mutant METTL3-METTL14 enzymes in a

552   20 µL reaction in the buffer containing 50 mM Tris pH 8.0, and 10 mM $MgCl_2$ and incubated at

553   room temperature. The reaction was excited at 320 nm with a 325 nm cut-off wavelength in a

554   SpectraMax M5 microplate reader (MolecularDevices). The fluorescence emission was measured

555   at 371 nm and 37°C every 5 minutes from 0 - 60 minutes and then every 30 minutes until the end

556   time point (120 minutes). The data were analyzed and fitted by GraphPad Prism (GraphPad

557   Software, San Diego, CA) using the Michaelis-Menten model (Y=Vmax*X/(Km+X), X = protein

558   concentration, Y = enzyme velocity, Vmax = maximum enzyme velocity, Km = Michaelis-Menten

559   constant). All results reported are mean values from three independent experiments with standard

560   deviations (s.d.) shown as error bars.

561

562   Surface plasmon resonance (SPR)

563   The surface plasmon resonance experiments were performed using a Biacore 1S+ equipped with

564   a CM5 sensor chip. Recombinant streptavidin (Millipore Sigma, 11721674001) was first

565   immobilized at all six flow cells using amine-coupling chemistry. The surfaces of flow cells were

566   activated for 7 min with a 1:1 mixture of 0.1 M NHS (N-hydroxysuccinimide) and 0.4 M EDC (3-

567   (N, N-dimethylamino) propyl-N-ethylcarbodiimide) at a flow rate of 10 µl/min. The streptavidin

568   at a concentration of 50 µg/ml in 10 mM sodium acetate, pH 5.5, was immobilized at a density of

569   around 6,000 RU on all six flow cells. All surfaces were blocked with a 7-minute injection of 1 M

570   ethanolamine, pH 8.0. The biotinyl-RNA substrates were then diluted to 100nM in running buffer

571   (10mM HEPES, 150mM KCl, 0.05% P20, pH 7.5) and captured in flow cell 3-6 respectively (12s,

572   5 µl/min) to reach a level around 50RU (see details below). To measure kinetic binding data, the

573   analytes (METTL3-METTL14$_{WT}$, METTL3-METTL14$_{R298P}$, and METTL3-METTL14$_{R471H}$

574   proteins) were diluted in the same running buffer, with five concentrations ranging from 2.4 to

575   1500 nM. The analytes were then injected over all flow cells at various concentrations in single-

576   cycle kinetics format at a flow rate of 30 µl/min at 25°C. The analyte was allowed to associate and

577   dissociate for 120 seconds for each injection and dissociate for 1200 seconds, respectively. Data

578   were collected at a rate of 10 Hz. The data were fit to a 1:1 binding model or two-state reaction

579   model, as mentioned, using the data analysis option available within Biacore Insight Evaluation

580   Software (Version 5.0.18.22102).

581

582   Molecular Dynamics Simulations

583   Structure preparation

584   The crystal structure of the METTL3-METTL14 complex bound to M^{6}A was used as the starting

585   point for all classical molecular dynamics simulations. The AlphaFold model of the METTL14

586   subunit (UniProt identifier: AF-Q3UIK4-F1) was integrated into the original crystal structure,

587   filling in the gaps and creating a refined METTL3-METTL14 enzyme structure that accounted for

588   the missing residues. Mutants T433A, K459A, R471H, H478A, E481A, and R298P were

589   generated using ICM-Pro software (www.molsoft.com). Additionally, the Δ472-473 and Δ472-474

590   deletions were obtained from the AlphaFold model. The refined structure was aligned to the crystal

591   structure (PDB ID: 7CV6), and the position of S-adenosyl-L-homocysteine was identified as the

592   initial position of m^6A for the m^6A-bound METTL3-METTL14 complex. The ProteinPrepare

593   module implemented in the PlayMolecule was employed to assign the protonation states of

594   residues at pH 7.0[48].

595

596   System setup and simulation protocol

597   The simulations were conducted using the Amberff14SB force field for the protein[49]. The m^6A was

598   subjected to geometry optimization using Gaussian 16 (HF/631G*) (www.gaussian.com). The

599   m^6A parameters were derived with GAFF as implemented in Ambertools23 using antechamber

600   and parmchk tools[50]. RESP partial charges were calculated with Gaussian 16 following the

601   procedure suggested by antechamber[51]. The preprocessed structure was explicitly solvated in a

602   cubic periodic of water molecules represented by the transferrable intermolecular potential with 3

603   points (TIP3P), whose boundary is at least 10 Å from any solute atoms so that the protein does not

604   interact with its periodic images. Periodic boundary conditions in all directions were utilized to

605   reduce the finite system size effects. To neutralize the total charge, Na^+/Cl^- counterions were

606   added. Subsequently, the systems were energy minimized by 5000 steps with the conjugate

607   gradient method to remove any local atomic clashes. Initial velocities within each simulation were

608   sampled from Boltzmann distribution at a temperature of 300 K. The solvents were equilibrated

609   for five ns under the NPT ensemble. The production simulations of supervised molecular dynamics

610   were run under the NVT ensemble using a Langevin thermostat with a damping of 0.1 ps^{-1} and

611   hydrogen mass repartitioning scheme to achieve time steps of 2 fs. Berendsen thermostat and

612   Langevin barostat were used to keep the temperature and pressure constant, respectively[52]. Long-

613   range electrostatic interactions were computed using the particle mesh Ewald summation

614   method[53]. The cutoff radius for neighbor searching and nonbonded interactions was taken to be 9

615   Å with a switching distance of 7.5 Å was used, and all bonds were constrained using the LINCS

616   algorithm[54]. In total, > 20 SuMD simulations were run as a swarm. Of these, the first three replicas

617   that met the supervision criteria were selected for analysis. All simulations were run using the

618   ACEMD engine[55].

619

620   Supervision procedure

621   Supervised molecular dynamics is a method that can accelerate the binding process between

622   ligands and protein recognition without introducing bias[56]. This method employs an algorithm that

623   monitors the distance between the ligand and the protein. Short simulations of specific lengths are

624   run, and the distance between the ligand and the protein is calculated. The fitting of linear least

625   squares is applied to fit the data, showing the distance against time. If the slope of the resulting

626   straight line is negative, indicating that the ligand is approaching the binding site, then the state of

627   the last frame, including the velocity and the coordinates of this short trajectory, will be used as

628   the initial state for the next short trajectory. On the contrary, if the slope is positive, thereby

629   indicating that the ligand is not approaching the binding site, the short trajectory will be discarded,

630   and the simulation will restart from the last initial state. However, to avoid the ligand being stuck,

631   assessed by 10 consecutive failed steps, a relatively longer simulation is run, followed by the final

632   state of the simulation being used as the starting point for the successive step. The supervision

633   algorithm is switched off when the distance reaches a defined threshold value. To explore the m^6A

634   swivel from substrate A binding pocket to product m^6A binding pocket, a supervision protocol was

635   designed in two steps. In the first step, during the production run of the MD trajectory, the distance

636 between the center of mass of the m^6A and the center of mass of the residues constituting the

637 product m^6A binding pocket (METTL3: I400, M402, T433, G434, R435, R471, T472, G473,

638 H474, H478, E481, and METTL14: R298) is monitored over a fixed time window (0.02ns). In the

639 second step, the distances between two key atom pairs were calculated, namely R298:NH1-

640 m^6A:N1 and H478:ND1-m^6A:P1. The trajectory analysis was carried out, and the figures were

641 made using PyMol (www.pymol.org) and VMD[57]. The graphs were made using Python scripts.

642

Data availability

644 The coding sequences of METTL3 (NCBI reference sequence GI: 33301371) and METTL14

645 (NCBI reference sequence GI: 172045930) used in this study are available at NCBI. We have

646 provided source data as a separate Source Data file. The atomic coordinates and structure factors

647 were deposited in the Protein Data Bank (PDB) under accession code 9DGJ (m6AMP) and DOI:

648 10.2210/pdb9dgj/pdb. The start files and the trajectories from molecular dynamics simulations can

649 be downloaded from https://doi.org/10.5281/zenodo.12681486. Requests for additional material

650 and information should be directly addressed to Y.K.G. (guptay@uthscsa.edu).

651

652

Figure legends

654 **Figure 1 | Structure of m⁶A bound human METTL3-METTL14 MTase core. a,** Domain

655 architecture of METTL3 and METTL14; and boundaries of each used in crystallization are shown

656 on top. Structure of the complex is shown in cartoon mode for METTL3 in cyan and METTL14

657 in orange; m6AMP (red) and interacting residues of METTL3 (green) and METTL14 (orange) are

658 shown in stick mode. Blue dot, the position of N^6 (in acceptor mode), i.e., ~3Å from the methyl

659 group of the donor SAM. Methylated N^6 of m⁶A is ~16Å away from its acceptor position in the

660 catalytic pocket (blue dot). Black dots, water. Black dashes, h-bonds. The panel on right shows a

661 close-up of the m⁶A interaction network, including the *arginine clasp.* **b,** An alignment of the

662 regions participating in m⁶A confirms strict conservation of the interaction network throughout the

663 evolution from yeast (Uniprot ID: P41833); arabidopsis (082486) and rice (Q6EU10); fruit fly

664 (Q9VCE6), zebrafish (F1R777), mouse (Q8C3P7), hamster (A0A1U7R3Z3), and monkey

665 (A0A8J8YGJ7); to human (Q86U44). **c,** Methyltransferase activity results of full-length human

666 METTL3-METTL14 (wild-type, WT) and eight mutant enzymes as derived from three

667 independent experiments, with error bars indicating the range of data points from these

668 experiments (n = 3). **d,** Quantitative measurement of RNA (red, m⁶A-RNA; blue, A-RNA) binding

669 (n = 3) by the WT enzyme shown as binding isotherms fitted with a one-site specific binding

670 model. The equilibrium dissociation constant or K_d derived for each mutant enzyme is plotted

671 along with K_d of the WT enzyme (**e**). ns, not significant (p >0.05), * denotes $p \leq 0.05$. Source data

672 for panels **c-e** are provided.

673

674 **Figure 2 | Enzyme and binding kinetics. a,** Methylation of NEAT2* RNA by full-length

675 METTL3-METTL14 (wild-type, WT and its mutants) at saturating concentrations of SAM and

676   RNA. **b-c,** Kinetics of RNA binding to the WT and mutant METTL3-METTL14 as measured

677   using surface plasmon resonance. Two RNA oligos (NEAT2* and a single-stranded RNA)

678   comprising substrate A (grey circle) or product m6A (red circle) were probed.

679

680   **Figure 3 | Base swiveling and loop orchestration. a-c,** Upper panels show overlays of regions of

681   METTL3 encompassing the catalytic motif, gate loops 1 and 2, and interface loop in METTL3

682   bound to m^{6}A (red stick), SAM (pink stick), and SAH (orange stick). Arrows indicate the

683   directional movement of loops. Lower panels: The entire region of each overlay is in stick mode.

684   Green dots, the residues that form the m^{6}A interaction network. **d,** Close-up of an overlay of m^{6}A

685   and apo MTase of METTL3-METTL14 shown in two orientations for clarity. The exit channel

686   between M402 and H474 in the m^{6}A bound conformation becomes wider (up to 8Å) to stabilize

687   m^{6}A and avoid steric clashes with its purine and ribose moieties. **e,** An overlay of MTase cores of

688   arabidopsis METTL4 (light blue cartoons)/SAH (light blue stick)/Am (blue stick) and METTL3

689   (cyan)-METTL14 (orange)/m^{6}A (red stick) clarifies the ~ 120º pivot of the base around phosphate.

690   Black dots, water molecules in the m^{6}A structure help stabilize the m^{6}A and compensate for the

691   loss in binding energy in the site emptied by base pivoting. **f,** Change in emission fluorescence

692   intensity upon titration of increasing concentration of WT (upper panel) and R298P mutant

693   enzymes (lower panel) with 2-aminopurine (2-Ap) containing RNA (n=3). See the methods section

694   and source data for details.

695

696   **Figure 4 | Mode of m^{6}A binding by writer/sensor, eraser, and reader.** Interaction networks of

697   m^{6}A (red) binding to METTL3 (green), and METTL14 (**a**), 6mA (blue) binding to FTO (**b**), and

698   m6A binding to YTH domain of YTHDC1 (**c**). The two nucleotides flanking the flipped methylated

699 base in FTO and YTHDC1 are shown in light blue and grey, respectively. The hydrophobic

700 stacking surface in YTHDC1 can only be aligned by rotating the molecule 180º around the x-axis,

701 suggesting that reader proteins approach RNA from the opposite direction. The m^{6}A pocket of

702 METTL3-METTL14 harbors features that enable it to act as an atypical m^{6}A sensor/reader during

703 its switch from writer to reader. Dashed lines, h-bonds.

704

705 **Movie 1 | Loop dynamics during conversion of A to m^{6}A and sensing by METTL3-METTL14**

706 An animation shows the motions in two gate loops and the interface loop of METTL3-METTL14.

707 The model for catalysis and m^{6}A sensing was generated by ChimeraX (UCSF). The position of A

708 during methylation is modeled by overlaying METTL3-SAM (PDB: 5IL1) with METTL4-Am

709 (PDB: 7CV6). The coordinates used for generating the morph movie are as follows: METTL3-

710 METTL14: m^{6}A (this study) apo (PDB: 5IL0), SAM (PDB: 5IL1), SAH (PDB: 5IL2).

711

712 Table 1. Capture level of different RNA substrates
713

Flow cell	RNA substrate	Captured (RU)
3	rNEAT2	66.4
4	rNEAT2-m6A	62.7
5	r6T	48.9
6	r6T-m6A	51.2

714

715 Table 2. Kinetic parameters for all evaluated bindings with 1:1 binding model
716

Ligand RNA	Analyte Protein	K_{on} (10^5 M^{-1} S^{-1})	K_{off} (10^{-2} S^{-1})	K_D (nM)	Rmax (RU_{max})
rNEAT2	METTL3-METTL14	1.64	4.22	256	5.19×10^2
rNEAT2-m6A	METTL3- METTL14	0.755	2.55	337	4.50×10^2
r6T	METTL3- METTL14	0.855	11.6	1360	4.21×10^2
r6T-m6A	METTL3- METTL14	0.0774	24100	3120	5.55×10^2

717

718 Table 3. Kinetic parameters for all evaluated bindings with two state reaction model
719

Ligand RNA	Analyte Protein	K_{on1} (M^{-1} S^{-1})	K_{off1} (S^{-1})	K_{on2} (M^{-1} S^{-1})	K_{off2} (S^{-1})	K_D(nM)	Rmax (RU_{max})
rNEAT2	R471H	2.59×10^4	2.17×10^{-2}	6.02×10^{-3}	4.54×10^{-4}	58.8	6.97×10^2
	R298P	2.93×10^4	2.28×10^{-2}	3.68×10^{-3}	3.11×10^{-3}	356	3.73×10^2
rNEAT2-m6A	R471H	2.73×10^4	2.22×10^{-2}	5.82×10^{-3}	4.85×10^{-4}	62.8	5.03×10^2
	R298P	2.38×10^4	2.77×10^{-2}	6.09×10^{-3}	5.23×10^{-3}	538	3.23×10^2
r6T	R471H	4.43×10^4	3.85×10^{-2}	5.06×10^{-3}	7.21×10^{-4}	108	4.19×10^2
	R298P	5.38×10^3	4.00×10^{-2}	2.14×10^{-3}	8.79×10^{-4}	2160	5.52×10^2
r6T-m6A	R471H	6.87×10^6	8.99	6.74×10^{-3}	1.01×10^{-3}	171	2.70×10^2
	R298P	6.62×10^2	3.66×10^{-2}	2.09×10^{-3}	1.48×10^{-3}	22900	2.47×10^3

720

721   **References**

722   1.   Bokar, J.A., Rath-Shambaugh, M.E., Ludwiczak, R., Narayan, P. & Rottman, F.
723   Characterization and partial purification of mRNA N6-adenosine methyltransferase from
724   HeLa cell nuclei. Internal mRNA methylation requires a multisubunit complex. *J Biol Chem*
725   **269**, 17697-704 (1994).
726   2.   Rottman, F.M., Bokar, J.A., Narayan, P., Shambaugh, M.E. & Ludwiczak, R. N6-adenosine
727   methylation in mRNA: substrate specificity and enzyme complexity. *Biochimie* **76**, 1109-
728   14 (1994).
729   3.   Meyer, K.D. et al. Comprehensive analysis of mRNA methylation reveals enrichment in 3'
730   UTRs and near stop codons. *Cell* **149**, 1635-46 (2012).
731   4.   Liu, J. et al. A METTL3-METTL14 complex mediates mammalian nuclear RNA N6-adenosine
732   methylation. *Nat Chem Biol* **10**, 93-5 (2014).
733   5.   Dominissini, D. et al. Topology of the human and mouse m6A RNA methylomes revealed
734   by m6A-seq. *Nature* **485**, 201-6 (2012).
735   6.   Liu, J. et al. N (6)-methyladenosine of chromosome-associated regulatory RNA regulates
736   chromatin state and transcription. *Science* **367**, 580-586 (2020).
737   7.   Ke, S. et al. m(6)A mRNA modifications are deposited in nascent pre-mRNA and are not
738   required for splicing but do specify cytoplasmic turnover. *Genes Dev* **31**, 990-1006 (2017).
739   8.   Perez-Pepe, M. et al. 7SK methylation by METTL3 promotes transcriptional activity. *Sci Adv*
740   **9**, eade7500 (2023).
741   9.   Bokar, J.A., Shambaugh, M.E., Polayes, D., Matera, A.G. & Rottman, F.M. Purification and
742   cDNA cloning of the AdoMet-binding subunit of the human mRNA (N6-adenosine)-
743   methyltransferase. *RNA* **3**, 1233-47 (1997).
744   10.   Bujnicki, J.M., Feder, M., Radlinska, M. & Blumenthal, R.M. Structure prediction and
745   phylogenetic analysis of a functionally diverse family of proteins homologous to the MT-
746   A70 subunit of the human mRNA:m(6)A methyltransferase. *J Mol Evol* **55**, 431-44 (2002).
747   11.   Woodcock, C.B. et al. Human MettL3-MettL14 complex is a sequence-specific DNA
748   adenine methyltransferase active on single-strand and unpaired DNA in vitro. *Cell Discov*
749   **5**, 63 (2019).
750   12.   Qi, S. et al. RNA binding to human METTL3-METTL14 restricts N(6)-deoxyadenosine
751   methylation of DNA in vitro. *Elife* **11**(2022).
752   13.   Woodcock, C.B., Horton, J.R., Zhang, X., Blumenthal, R.M. & Cheng, X. Beta class amino
753   methyltransferases from bacteria to humans: evolution and structural consequences.
754   *Nucleic Acids Res* **48**, 10034-10044 (2020).
755   14.   Wang, X. et al. Structural basis of N(6)-adenosine methylation by the METTL3-METTL14
756   complex. *Nature* **534**, 575-8 (2016).
757   15.   Wang, P., Doxtader, K.A. & Nam, Y. Structural Basis for Cooperative Function of Mettl3 and
758   Mettl14 Methyltransferases. *Mol Cell* **63**, 306-17 (2016).
759   16.   Sledz, P. & Jinek, M. Structural insights into the molecular mechanism of the m(6)A writer
760   complex. *Elife* **5**(2016).
761   17.   Wang, Y. et al. N6-methyladenosine modification destabilizes developmental regulators in
762   embryonic stem cells. *Nat Cell Biol* **16**, 191-8 (2014).

763 18. Shi, H., Wei, J. & He, C. Where, When, and How: Context-Dependent Functions of RNA
764   Methylation Writers, Readers, and Erasers. *Mol Cell* **74**, 640-650 (2019).
765 19. Flamand, M.N., Tegowski, M. & Meyer, K.D. The Proteins of mRNA Modification: Writers,
766   Readers, and Erasers. *Annu Rev Biochem* **92**, 145-173 (2023).
767 20. Geula, S. et al. Stem cells. m6A mRNA methylation facilitates resolution of naive
768   pluripotency toward differentiation. *Science* **347**, 1002-6 (2015).
769 21. Wu, Y. et al. Mettl3-mediated m(6)A RNA methylation regulates the fate of bone marrow
770   mesenchymal stem cells and osteoporosis. *Nat Commun* **9**, 4772 (2018).
771 22. Wang, Y. et al. N(6)-methyladenosine RNA modification regulates embryonic neural stem
772   cell self-renewal through histone modifications. *Nat Neurosci* **21**, 195-206 (2018).
773 23. Lin, S., Choe, J., Du, P., Triboulet, R. & Gregory, R.I. The m(6)A Methyltransferase METTL3
774   Promotes Translation in Human Cancer Cells. *Mol Cell* **62**, 335-45 (2016).
775 24. Barbieri, I. et al. Promoter-bound METTL3 maintains myeloid leukaemia by m(6)A-
776   dependent translation control. *Nature* **552**, 126-131 (2017).
777 25. Choe, J. et al. mRNA circularization by METTL3-eIF3h enhances translation and promotes
778   oncogenesis. *Nature* **561**, 556-560 (2018).
779 26. Yankova, E. et al. Small-molecule inhibition of METTL3 as a strategy against myeloid
780   leukaemia. *Nature* **593**, 597-601 (2021).
781 27. McFadden, M.J. & Horner, S.M. N(6)-Methyladenosine Regulates Host Responses to Viral
782   Infection. *Trends Biochem Sci* **46**, 366-377 (2021).
783 28. Burgess, H.M. et al. Targeting the m(6)A RNA modification pathway blocks SARS-CoV-2 and
784   HCoV-OC43 replication. *Genes Dev* **35**, 1005-1019 (2021).
785 29. Li, N. et al. METTL3 regulates viral m6A RNA modification and host cell innate immune
786   responses during SARS-CoV-2 infection. *Cell Rep* **35**, 109091 (2021).
787 30. Vu, L.P. et al. The N6-methyladenosine (m6A)-forming enzyme METTL3 controls myeloid
788   differentiation of normal hematopoietic and leukemia cells. *Nat Med* (2017).
789 31. Schumann, U., Shafik, A. & Preiss, T. METTL3 Gains R/W Access to the Epitranscriptome.
790   *Mol Cell* **62**, 323-324 (2016).
791 32. Forbes, S.A. et al. COSMIC: exploring the world's knowledge of somatic mutations in
792   human cancer. *Nucleic Acids Res* **43**, D805-11 (2015).
793 33. Liu, J. et al. m(6)A mRNA methylation regulates AKT activity to promote the proliferation
794   and tumorigenicity of endometrial cancer. *Nat Cell Biol* **20**, 1074-1083 (2018).
795 34. Coots, R.A. et al. m(6)A Facilitates eIF4F-Independent mRNA Translation. *Mol Cell* **68**, 504-
796   514 e7 (2017).
797 35. Zhang, C. et al. Cancer mutations rewire the RNA methylation specificity of METTL3-
798   METTL14. *bioRxiv* (2023).
799 36. Luo, Q. et al. Structural insights into molecular mechanism for N(6)-adenosine
800   methylation by MT-A70 family methyltransferase METTL4. *Nat Commun* **13**, 5636 (2022).
801 37. Gupta, Y.K., Chan, S.H., Xu, S.Y. & Aggarwal, A.K. Structural basis of asymmetric DNA
802   methylation and ATP-triggered long-range diffusion by EcoP15I. *Nat Commun* **6**, 7363
803   (2015).
804 38. Zhang, X. et al. Structural insights into FTO's catalytic mechanism for the demethylation
805   of multiple RNA substrates. *Proc Natl Acad Sci U S A* **116**, 2919-2924 (2019).

806 39. Mauer, J. et al. Reversible methylation of m(6)A(m) in the 5' cap controls mRNA stability.
807   *Nature* **541**, 371-375 (2017).
808 40. Xu, C. et al. Structural basis for selective binding of m6A RNA by the YTHDC1 YTH domain.
809   *Nat Chem Biol* **10**, 927-9 (2014).
810 41. Allan, B.W. & Reich, N.O. Targeted base stacking disruption by the EcoRI DNA
811   methyltransferase. *Biochemistry* **35**, 14757-62 (1996).
812 42. Hamdane, D., Guelorget, A., Guerineau, V. & Golinelli-Pimpaneau, B. Dynamics of RNA
813   modification by a multi-site-specific tRNA methyltransferase. *Nucleic Acids Res* **42**, 11697-
814   706 (2014).
815 43. Smart, O.S. et al. Validation of ligands in macromolecular structures determined by X-ray
816   crystallography. *Acta Crystallogr D Struct Biol* **74**, 228-236 (2018).
817 44. Corbeski, I. et al. The catalytic mechanism of the RNA methyltransferase METTL3. *Elife*
818   **12**(2024).
819 45. Adams, P.D. et al. PHENIX: a comprehensive Python-based system for macromolecular
820   structure solution. *Acta Crystallogr D Biol Crystallogr* **66**, 213-21 (2010).
821 46. Emsley, P. & Cowtan, K. Coot: model-building tools for molecular graphics. *Acta Crystallogr*
822   *D Biol Crystallogr* **60**, 2126-32 (2004).
823 47. Bricogne G., B.E., Brandl M., Flensburg C., Keller P., Paciorek W., & Roversi P, S.A., Smart
824   O.S., Vonrhein C., Womack T.O. BUSTER version 2.10.4. Cambridge, United Kingdom:
825   Global Phasing Ltd. (2017).
826 48. Martinez-Rosell, G., Giorgino, T. & De Fabritiis, G. PlayMolecule ProteinPrepare: A Web
827   Application for Protein Preparation for Molecular Dynamics Simulations. *J Chem Inf Model*
828   **57**, 1511-1516 (2017).
829 49. Maier, J.A. et al. ff14SB: Improving the Accuracy of Protein Side Chain and Backbone
830   Parameters from ff99SB. *J Chem Theory Comput* **11**, 3696-713 (2015).
831 50. Case, D.A. et al. AmberTools. *J Chem Inf Model* **63**, 6183-6191 (2023).
832 51. Wang, J., Wang, W., Kollman, P.A. & Case, D.A. Automatic atom type and bond type
833   perception in molecular mechanical calculations. *J Mol Graph Model* **25**, 247-60 (2006).
834 52. Hoover, W.G., Ladd, A.J.C. & Moran, B. High-Strain-Rate Plastic Flow Studied via
835   Nonequilibrium Molecular Dynamics. *Physical Review Letters* **48**, 1818-1820 (1982).
836 53. Cerutti, D.S., Duke, R.E., Darden, T.A. & Lybrand, T.P. Staggered Mesh Ewald: An extension
837   of the Smooth Particle-Mesh Ewald method adding great versatility. *J Chem Theory*
838   *Comput* **5**, 2322 (2009).
839 54. Hess, B., Bekker, H., Berendsen, H.J.C. & Fraaije, J.G.E.M. LINCS: A linear constraint solver
840   for molecular simulations. *Journal of Computational Chemistry* **18**, 1463-1472 (1997).
841 55. Doerr, S., Harvey, M.J., Noé, F. & De Fabritiis, G. HTMD: High-Throughput Molecular
842   Dynamics for Molecular Discovery. *Journal of Chemical Theory and Computation* **12**, 1845-
843   1852 (2016).
844 56. Sabbadin, D. & Moro, S. Supervised Molecular Dynamics (SuMD) as a Helpful Tool To
845   Depict GPCR–Ligand Recognition Pathway in a Nanosecond Time Scale. *Journal of*
846   *Chemical Information and Modeling* **54**, 372-376 (2014).
847 57. Humphrey, W., Dalke, A. & Schulten, K. VMD: visual molecular dynamics. *J Mol Graph* **14**,
848   33-8, 27-8 (1996).
849

860 **Author contributions**

861 Y.K.G. conceived, designed, and supervised the overall study; S.Q. A.K. purified proteins and

862 performed biochemical assays. M.P., C.V., and N.G. assisted with protein purification. S.Q.

863 performed crystallography. S.Z. performed SPR experiments. S.C. and S.H. performed molecular

864 dynamics. S.H.C., M.K.R., and S.F.M. provided critical reagents. S.Q, A.K., S.C, S.Z., S.H., and

865 Y.K.G. analyzed data. Y.K.G. wrote the manuscript with input from all authors. All authors

866 approved this version.

867

868 **Competing interests**

869 Y.K.G is the founder of Atomic Therapeutics. S-H.C. is an employee of New England Biolabs.

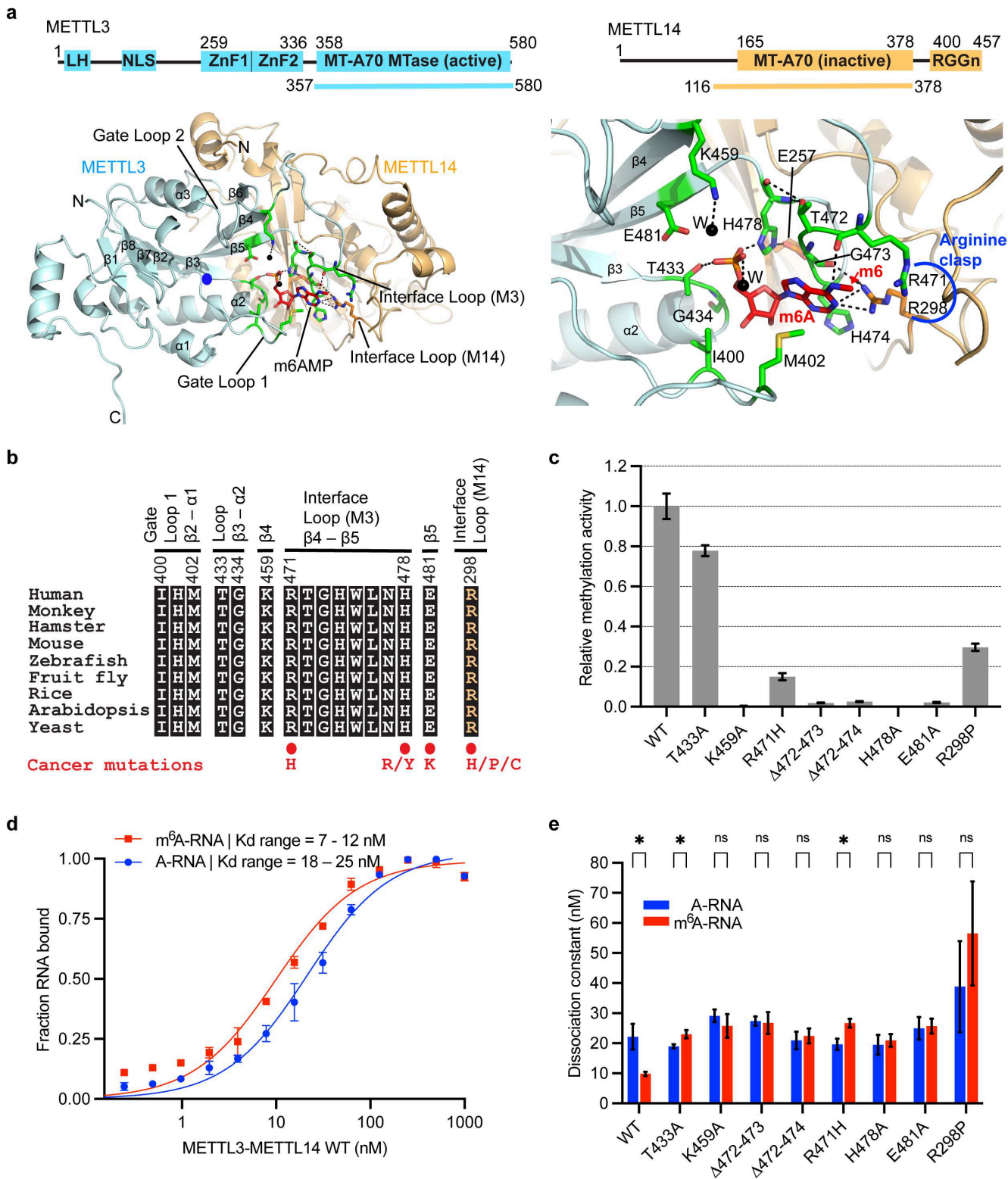**870** These affiliations do not affect the authors's impartiality and adherence to the journal's standards.

871

872 **Materials and correspondence**

873   Correspondence and requests for material should be addressed to Y.K.G. (Email:

874   guptay@uthscsa.edu).

Figures

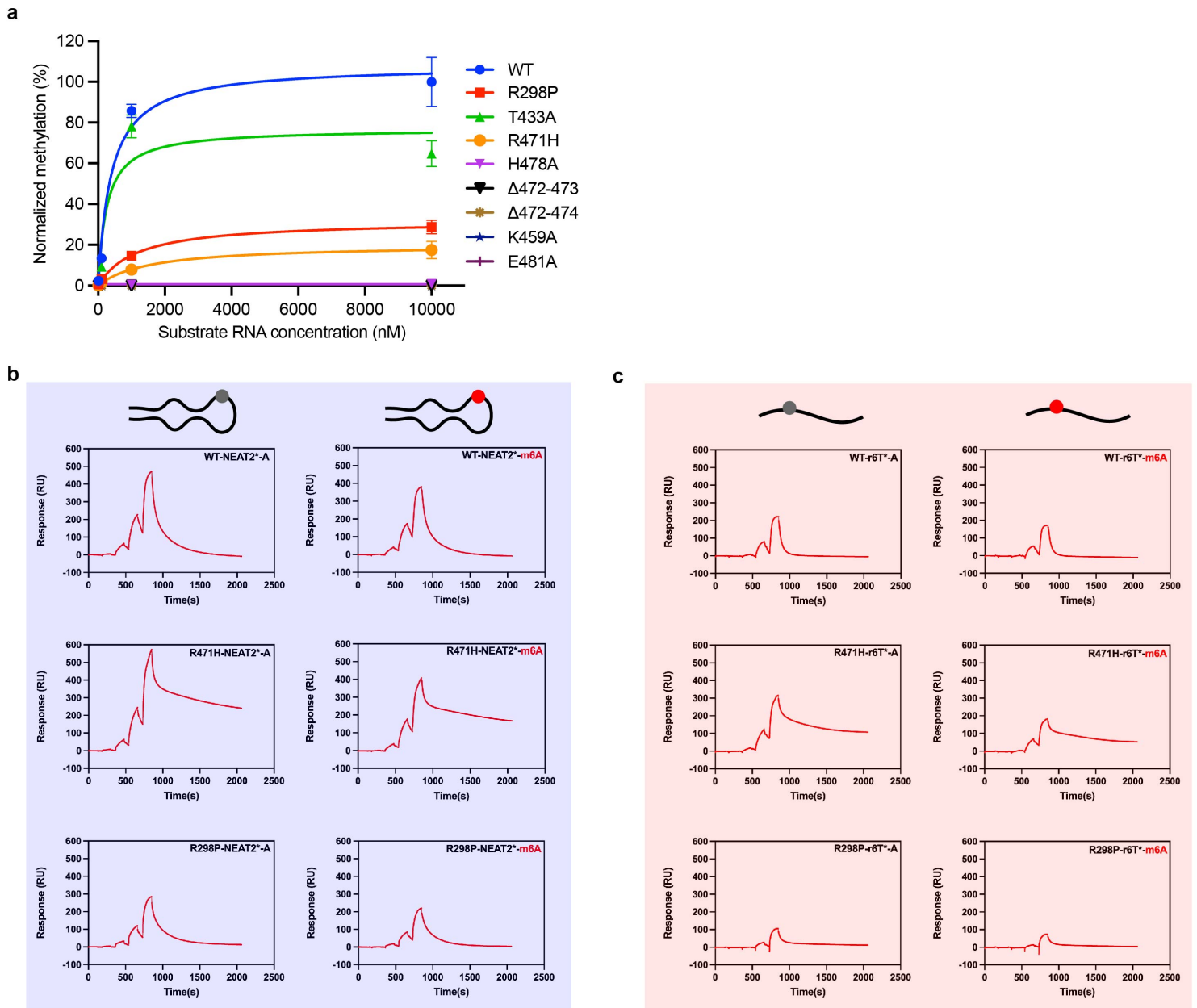## Figure 1

Structure of m⁶A bound human METTL3-METTL14 MTase core. a, Domain architecture of METTL3 and METTL14; and boundaries of each used in crystallization are shown on top. Structure of the complex is shown in cartoon mode for METTL3 in cyan and METTL14 in orange; m6AMP (red) and interacting

residues of METTL3 (green) and METTL14 (orange) are shown in stick mode. Blue dot, the position of N^6 (in acceptor mode), i.e., ~3Å from the methyl group of the donor SAM. Methylated N^6 of m^{6}A is ~16Å away from its acceptor position in the catalytic pocket (blue dot). Black dots, water. Black dashes, h-bonds. The panel on right shows a close-up of the m^{6}A interaction network, including the *arginine clasp.* **b,** An alignment of the regions participating in m^{6}A confirms strict conservation of the interaction network throughout the evolution from yeast (Uniprot ID: P41833); arabidopsis (082486) and rice (Q6EU10); fruit fly (Q9VCE6), zebrafish (F1R777), mouse (Q8C3P7), hamster (A0A1U7R3Z3), and monkey (A0A8J8YGJ7); to human (Q86U44). **c,** Methyltransferase activity results of full-length human METTL3-METTL14 (wild-type, WT) and eight mutant enzymes as derived from three independent experiments, with error bars indicating the range of data points from these experiments (n = 3). **d,** Quantitative measurement of RNA (red, m^{6}A-RNA; blue, A-RNA) binding (n = 3) by the WT enzyme shown as binding isotherms fitted with a one-site specific binding model. The equilibrium dissociation constant or K_d derived for each mutant enzyme is plotted along with K_d of the WT enzyme (**e**). ns, not significant (p >0.05), * denotes $p \leq 0.05$. Source data for panels **c-e** are provided.
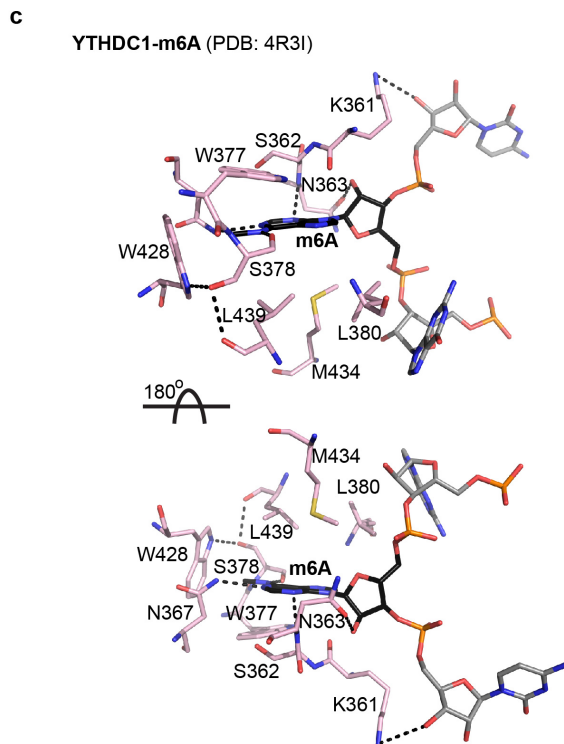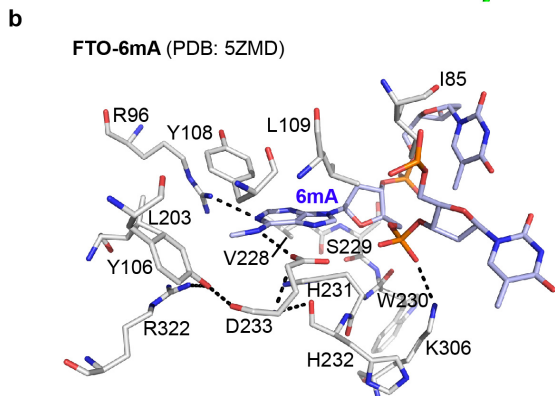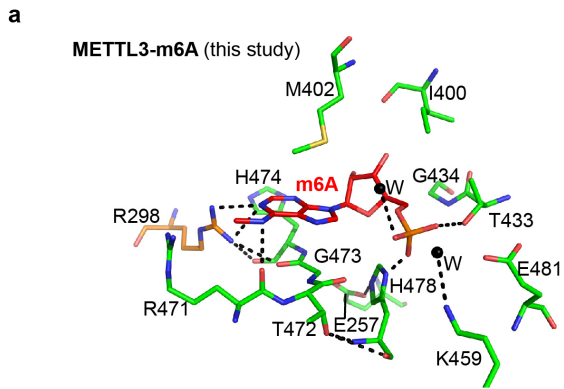
Figure 2

Enzyme and binding kinetics. a, Methylation of NEAT2* RNA by full-length METTL3-METTL14 (wild-type, WT and its mutants) at saturating concentrations of SAM and RNA. **b-c,** Kinetics of RNA binding to the WT and mutant METTL3-METTL14 as measured using surface plasmon resonance. Two RNA oligos (NEAT2* and a single-stranded RNA) comprising substrate A (grey circle) or product m6A (red circle) were probed.
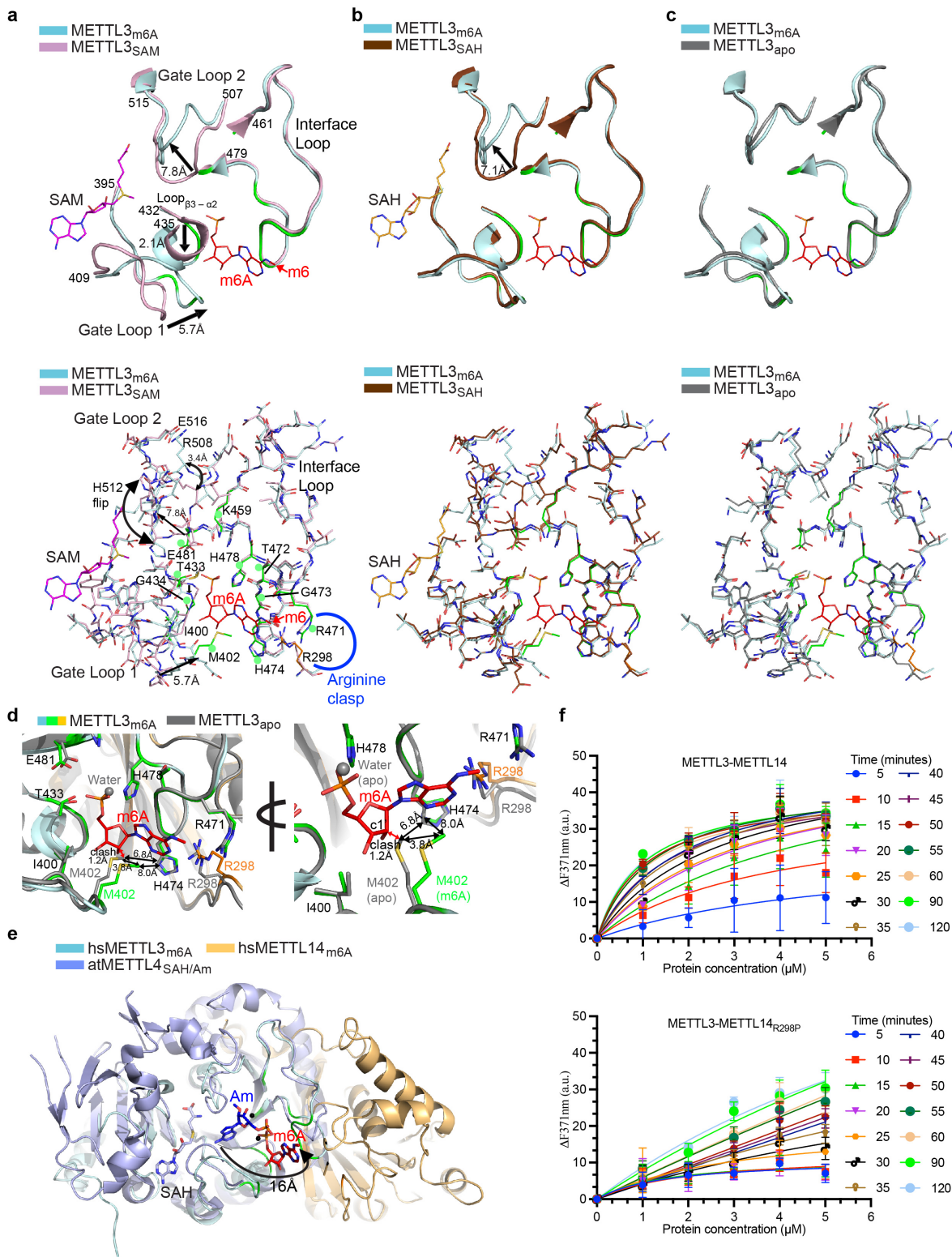
Figure 3

Base swiveling and loop orchestration. a-c, Upper panels show overlays of regions of METTL3 encompassing the catalytic motif, gate loops 1 and 2, and interface loop in METTL3 bound to m^6A (red stick), SAM (pink stick), and SAH (orange stick). Arrows indicate the directional movement of loops. Lower panels: The entire region of each overlay is in stick mode. Green dots, the residues that form the m^6A interaction network. **d,** Close-up of an overlay of m^6A and apo MTase of METTL3-METTL14 shown

in two orientations for clarity. The exit channel between M402 and H474 in the m^{6}A bound conformation becomes wider (up to 8Å) to stabilize m^{6}A and avoid steric clashes with its purine and ribose moieties. **e,** An overlay of MTase cores of arabidopsis METTL4 (light blue cartoons)/SAH (light blue stick)/Am (blue stick) and METTL3 (cyan)-METTL14 (orange)/m^{6}A (red stick) clarifies the ~ 120º pivot of the base around phosphate. Black dots, water molecules in the m^{6}A structure help stabilize the m^{6}A and compensate for the loss in binding energy in the site emptied by base pivoting. **f,** Change in emission fluorescence intensity upon titration of increasing concentration of WT (upper panel) and R298P mutant enzymes (lower panel) with 2-aminopurine (2-Ap) containing RNA (n=3). See the methods section and source data for details.

a

METTL3-m6A (this study)

M402   I400

H474   m6A   G434

R298   W   T433

G473

R471   T472   E257   H478   W   E481

K459

b

FTO-6mA (PDB: 5ZMD)

I85

R96   Y108   L109

6mA

L203   V228   S229

Y106   H231   W230

R322   D233   H232   K306

c

YTHDC1-m6A (PDB: 4R3I)

K361

S362

W377

N363

m6A

W428   S378

L439

L380

M434

180°

M434

L380

L439

W428   S378   m6A

N367   W377   N363

S362

K361

Figure 4

Mode of m⁶A binding by writer/sensor, eraser, and reader. Interaction networks of m^6A (red) binding to METTL3 (green), and METTL14 (**a**), 6mA (blue) binding to FTO (**b**), and m6A binding to YTH domain of YTHDC1 (**c**). The two nucleotides flanking the flipped methylated base in FTO and YTHDC1 are shown in light blue and grey, respectively. The hydrophobic stacking surface in YTHDC1 can only be aligned by rotating the molecule 180° around the x-axis, suggesting that reader proteins approach RNA from the

opposite direction. The m^{6}A pocket of METTL3-METTL14 harbors features that enable it to act as an atypical m^{6}A sensor/reader during its switch from writer to reader. Dashed lines, h-bonds.

Supplementary Files

This is a list of supplementary files associated with this preprint. Click to download.

- ExtendeddataeLife101524.pdf
- D1000288066valreportfullP11.pdf
- m6amoviecaptionthinnerarrow.mov